

Geochemistry, Geophysics, Geosystems

Supporting Information for

Geodynamic and isotopic constraints on the genesis of kimberlites, lamproites and related magmas from the Finnish segment of the Karelian craton

Hayden Dalton¹, Andrea Giuliani^{1,2}, Janet Hergt¹, David Phillips¹, Hugh O'Brien³, Maxim D. Ballmer⁴, Roland Maas¹, Jon Woodhead¹

¹ KiDs (Kimberlites and Diamonds) Research Group, School of Geography, Earth and Atmospheric Sciences, The University of Melbourne, Parkville, 3010 Victoria, Australia

Corresponding author: Hayden Dalton (hayden.dalton@unimelb.edu.au)

² Institute of Geochemistry and Petrology, Department of Earth Sciences, ETH Zurich, Clausiusstrasse 25, Zurich 8092, Switzerland

³ Geological Survey of Finland, P.O. Box 96, Espoo, Finland

⁴ Department of Earth Sciences, University College London, London, UK

Contents of this file

**Text S1
Figures S1 to S9
Tables S1 to S2**

Introduction

The following document contains supplementary text outlining our geothermometric modelling to supplement that provided in section 5.3.1 in the main text. It also includes a number of supplementary figures.

Text S1.

To estimate variations in lithospheric thickness across the Kaavi-Kuopio field, we have estimated pressure and temperature of equilibration of clinopyroxene xenocrysts (data

from Lehtonen and O'Brien, 2009; Peltonen et al., 1999) using the thermobarometer of Nimis and Taylor (2000) and calculated corresponding paleogeotherms with FITPLOT (Mather et al., 2011). Clinopyroxene-based paleogeotherms for Pipes 2, 3, 5, 7, 9, 10 and 14 suggest there is apparently some variability in lithospheric thickness beneath these bodies (Supp.Fig. S3). Although the clinopyroxene data are limited for some bodies (Pipes 9, 10 and 14), there appears to be no clear relationship between lithospheric thickness and isotopic composition (Supp.Fig. S3H). This lack of relationship is exemplified by Pipe 2 and Pipe 3 which are geographically adjacent and petrographically nearly identical (Fig. 1, main text), have traversed lithospheric columns of very similar thickness (Supp.Fig. S3), yet have distinct isotopic signatures ($\epsilon\text{Hf}_{(i)}$) of +0.4 for Pipe 2 and -3.9 for Pipe 3; Fig. 2, main text; Supp.Fig. S3).

To evaluate the potential role of temperature in explaining the observed inter-pipe $\epsilon\text{Hf}_{(i)}$ variability we have applied the olivine-chromite Fe-Mg exchange geothermometer (Ballhaus et al., 1994; Fedortchouk and Canil, 2004; O'Neill and Wall, 1987) to the Kaavi-Kuopio samples. To apply this geothermometer to samples lacking fresh olivine, we have calculated olivine rim Mg# values for Pipes 2, 3 and 10 using the linear relationship between chromite Mg# and olivine rim Mg# observed in the Kaavi-Kuopio kimberlites (Supp.Table S1; Dalton et al., 2020). This approach provides temperatures ranging from ~1240 °C (Pipe 14) to ~1140 °C (Pipe 10) with typical uncertainties of ± 50 °C (Fedortchouk and Canil, 2004; Supp. Table. S1; Supp.Fig. S4). Importantly, these values do account for the thermal effects of mantle assimilation, an endothermic process that is known to influence the major element composition of these melts (e.g., Dalton et

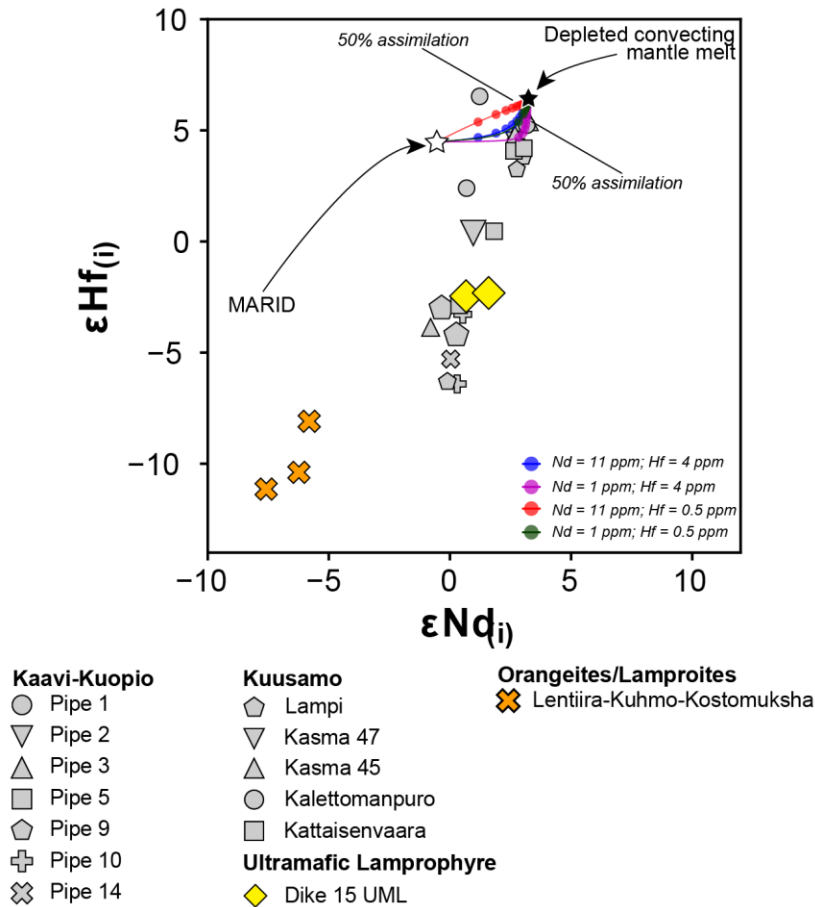
al., 2020a). To estimate the relative decrease in melt temperature associated with bulk assimilation of mantle peridotite wall rocks we have employed the following equation [1], which is modified from Kavanagh and Sparks (2009).

$$[1] \quad T_{Kimb} = \frac{(T_e \times (f \times C_{p,WR} + (1-f) \times C_{p,Kim}) + f \times L_{WR} - f \times T_{WR} \times C_{p,WR})}{((1-f) \times C_{p,Kim})}$$

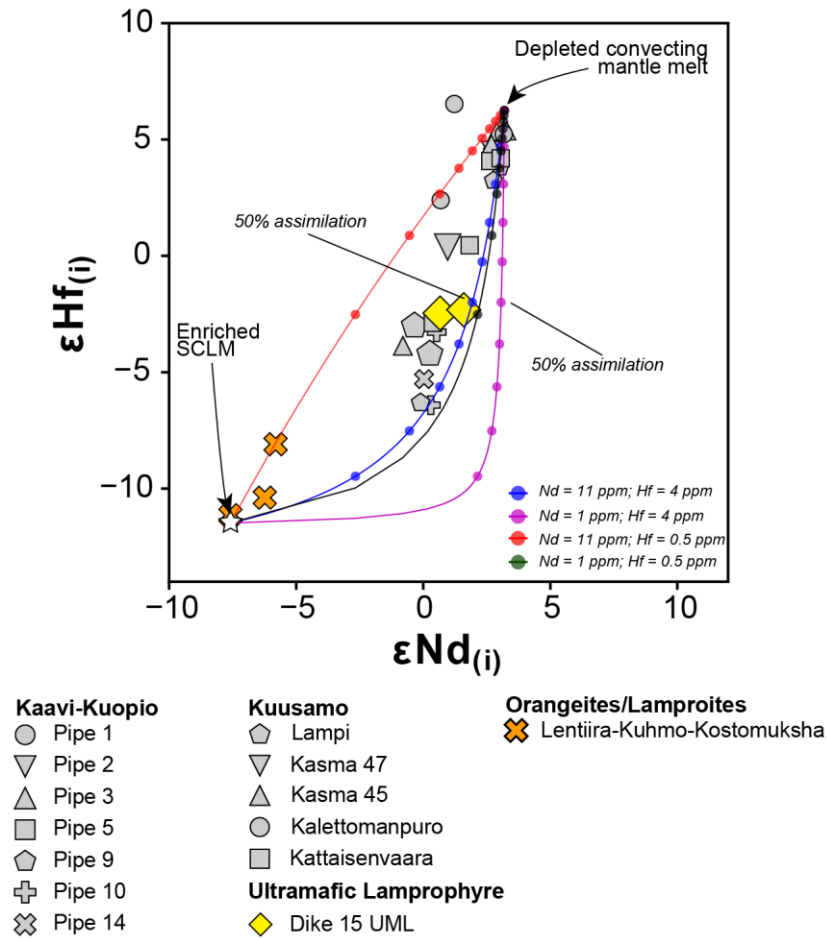
Where T_{Kimb} = temperature (K) of kimberlite melt prior to assimilation of mantle peridotite; T_e = equilibrium temperature (K) of kimberlite after peridotite assimilation, calculated from the olivine-chromite Fe-Mg exchange thermometer; f = fraction of mantle peridotite assimilated; $C_{p,WR}$ = specific heat capacity of whole-rock peridotite (1200 J kg⁻¹ K⁻¹); $C_{p,Kim}$ = specific heat capacity of kimberlite (1600 J kg⁻¹ K⁻¹); L_{WR} = latent heat of whole-rock peridotite (600000 J kg⁻¹).

It is difficult to place accurate constraints on the volume/fraction of peridotite material assimilated by an ascending kimberlite. Recent calculations predict that less than 15% (by mass) of orthopyroxene can be dissolved by kimberlites (Giuliani et al., 2020) while estimates of bulk peridotite assimilation based on bulk-kimberlite PGE concentrations vary between 5 and 35 vol.% for dikes of the Premier kimberlite (Tappe et al., 2020). Here we estimate volume fraction of assimilation using the orthopyroxene dissolution calculations of Giuliani et al. (2020b) applied to each Kaavi-Kuopio kimberlite (Supp. Table S1). Whilst significant uncertainty may exist in the absolute estimates of assimilation volumes, we stress that the relative differences among the Kaavi-Kuopio kimberlites of importance here. We observe no simple relationship between temperature (either before or after lithospheric mantle assimilation) and $\epsilon Hf_{(i)}$ (Supp. Fig. S4). In

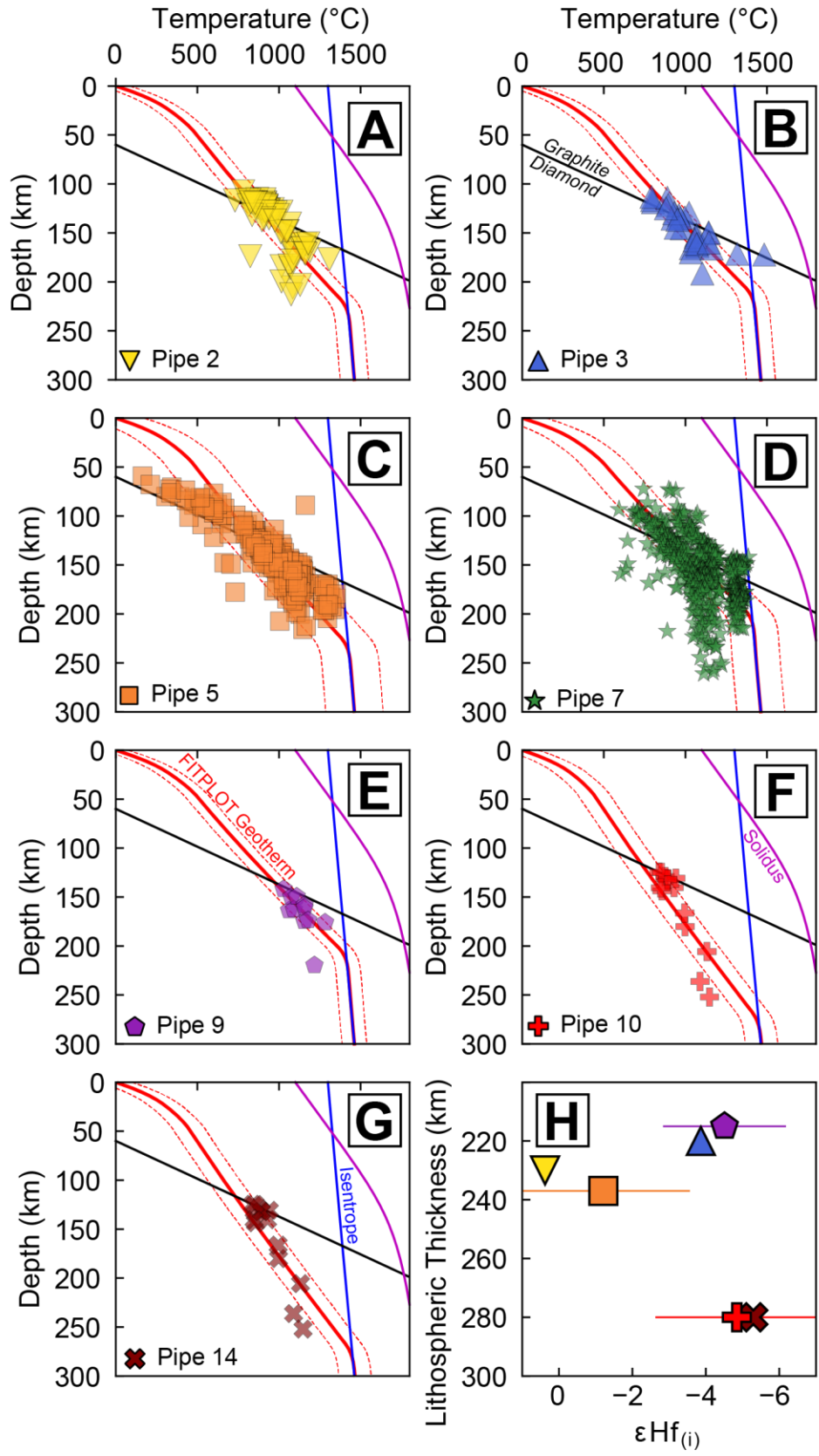
summary, it is evident that $\epsilon_{\text{Hf}(i)}$ variations in the Kaavi-Kuopio kimberlites cannot be readily explained by differences in melting temperature.



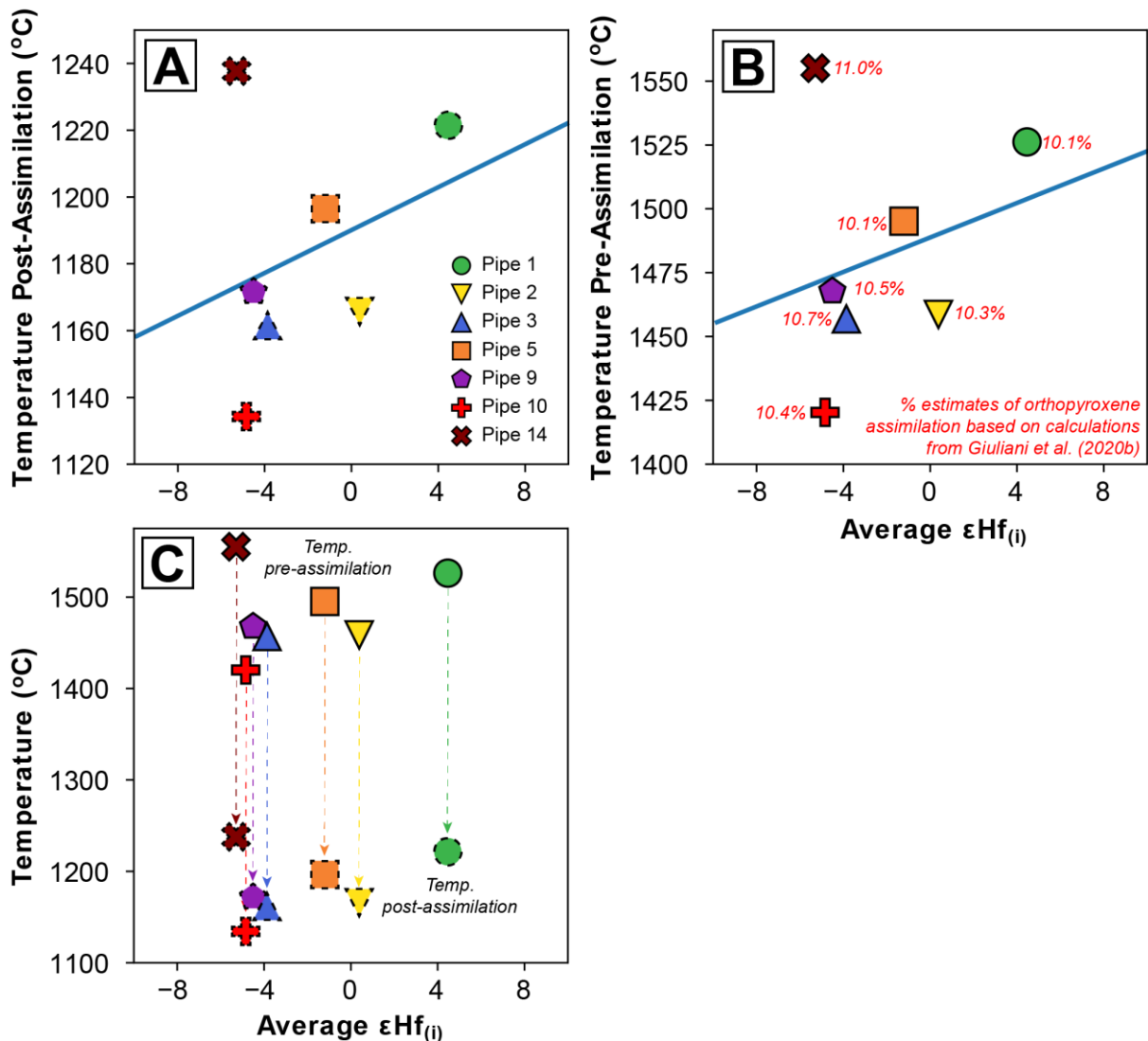
Supplementary Figure S1. Bivariate plot of $\epsilon_{\text{Hf}(i)}$ vs $\epsilon_{\text{Nd}(i)}$ showing a binary mixing relationship a geochemically depleted asthenospheric melt (composition from the PREMA reservoir of Tovey et al. (2021)) and increasing proportions of MARID-like, enriched lithospheric mantle (isotopic composition from Fitzpayne et al. (2019), trace element abundances from range presented by Gregoire et al. (2002) and Fitzpayne et al. (2018)). See Supplementary Table S2 for model parameters.



Supplementary Figure S2. Bivariate plot of $\epsilon_{\text{Hf}(i)}$ vs $\epsilon_{\text{Nd}(i)}$ showing a binary mixing relationship a geochemically depleted asthenospheric melt (composition from the PREMA reservoir of Tovey et al. (2021)) and increasing proportions of MARID-like, enriched lithospheric mantle (isotopic composition from olivine lamproites in this study, taken as proxy for composition of local metasomatised lithospheric mantle) and trace element abundances from range presented by Gregoire et al. (2002) and Fitzpayne et al. (2018)). See Supplementary Table S2 for model parameters.

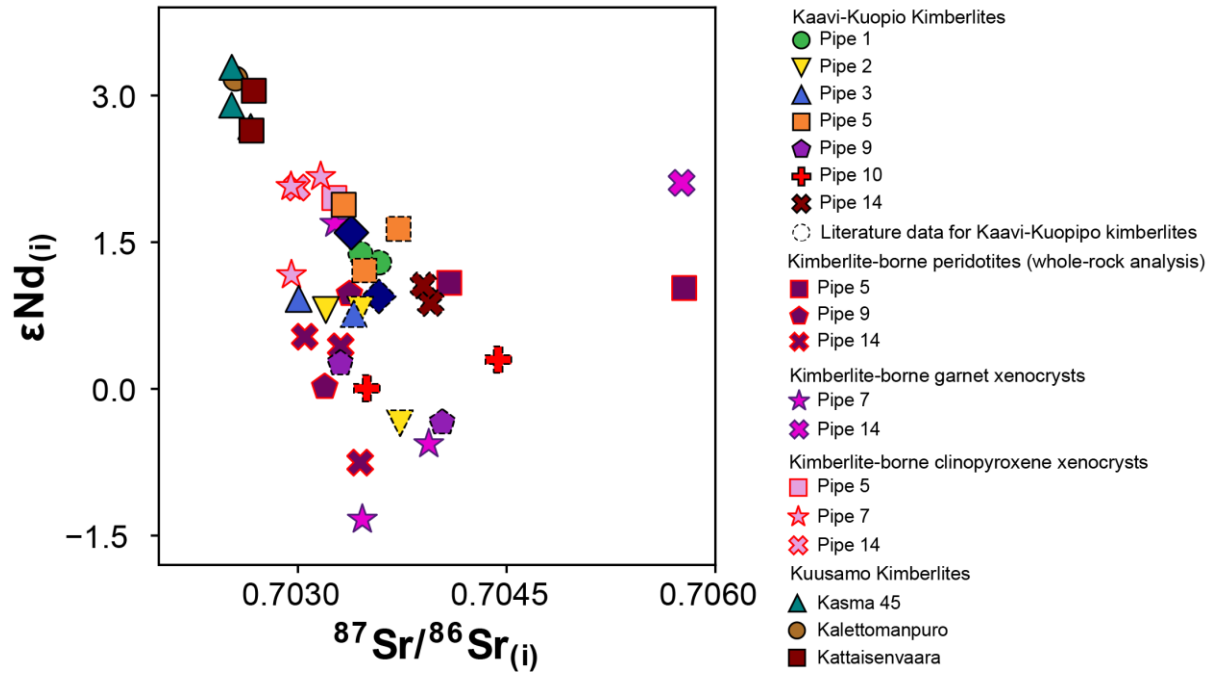


Supplementary Figure S3: (A-G) Plots of P-T data for clinopyroxene xenocrysts from the Kaavi-Kuopio kimberlites and (H) a comparison of lithospheric thickness beneath each kimberlite with average kimberlite $\epsilon\text{Hf}_{(i)}$ compositions. A) Pipe 2; B) Pipe 3; C) Pipe 5; D) Pipe 7; E) Pipe 9; F) Pipe 10; G) Pipe 14; H) Lithospheric thickness, as calculated from A-G, vs. average $\epsilon\text{Hf}_{(i)}$ compositions for each kimberlite. P-T conditions calculated using the thermobarometer of Nimis and Taylor (2000) and clinopyroxene data from Lehtonen and O'Brien (2009) and Peltonen et al. (1999). Paleogeotherms derived using FITPLOT (Mather et al., 2011) assuming a heat flow of 36 mW/m² and an isentrope of 1300 °C.

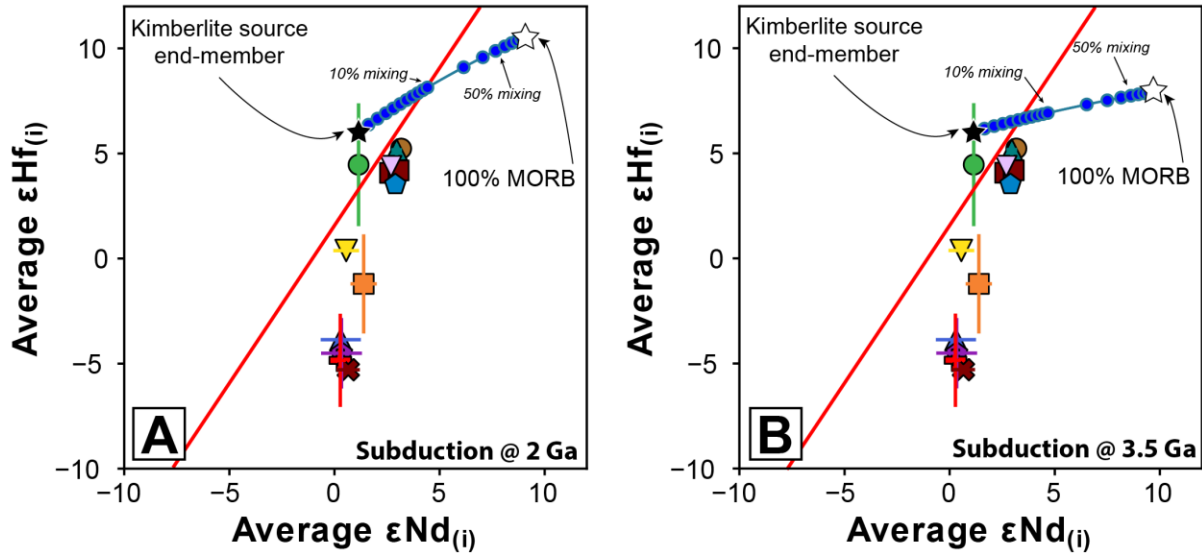


Supplementary Figure S4: Plots of kimberlite melt temperatures and $\epsilon\text{Hf}_{(i)}$ compositions for the Kaavi-Kuopio kimberlites. A) Kimberlite melt temperature vs $\epsilon\text{Hf}_{(i)}$ where temperatures are calculated based on olivine-chromite Fe-Mg exchange geothermometer (Ballhaus et al., 1994; Fedortchouk and Canil, 2004; O'Neill and Wall, 1987) and represents the physical conditions after assimilation

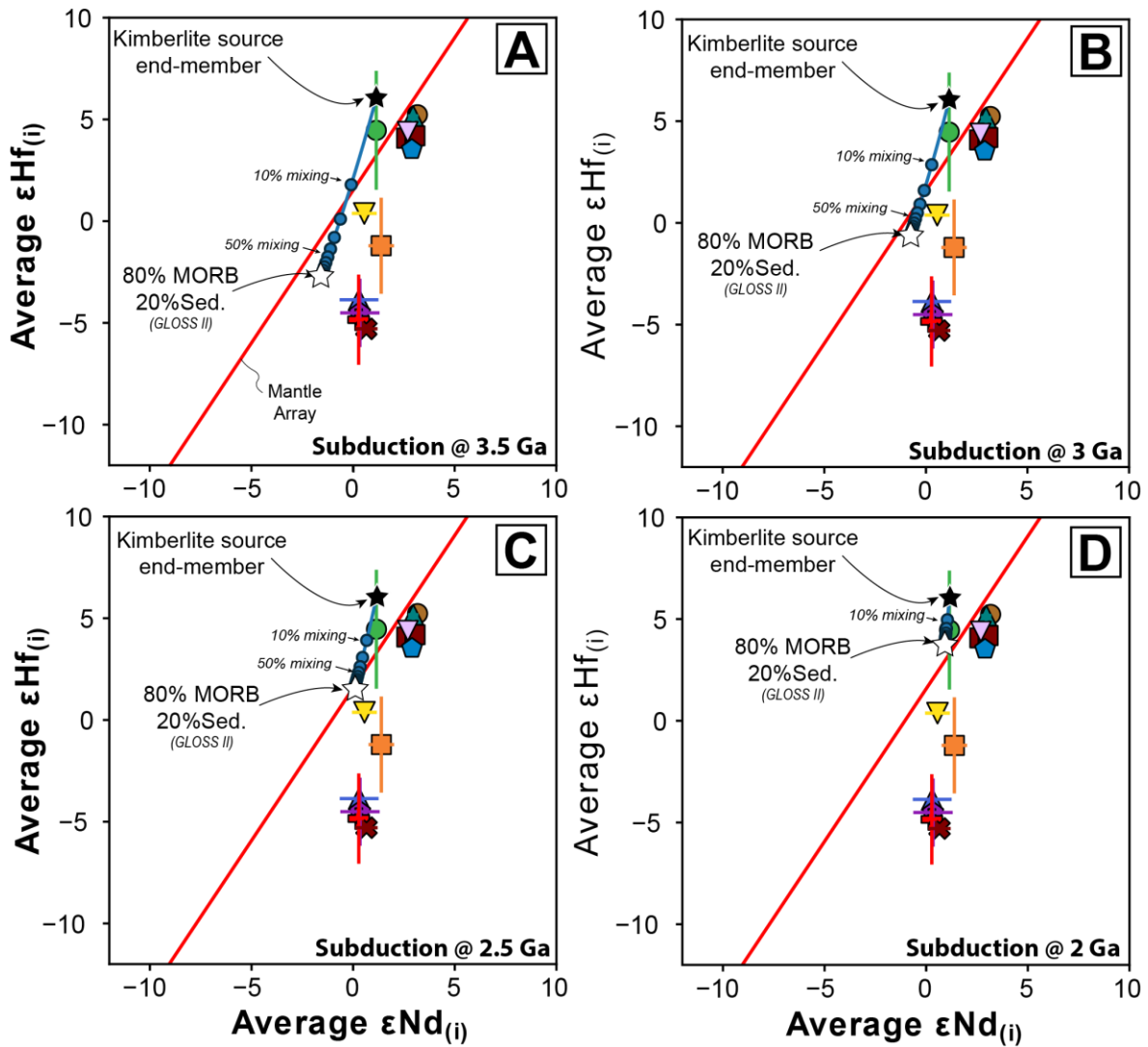
of peridotitic wall-rock; B) Kimberlite melt temperature vs $\epsilon Hf_{(i)}$, where the temperature is corrected for assimilation based on estimates for the fraction (%) of orthopyroxene assimilated and using equation [1]; orthopyroxene assimilation estimates calculated using the formulation of Giuliani et al. (2020); C) Plots A & B overlay with arrows to indicate change in temperature before and after assimilation. All values presented in Supplementary Table S1



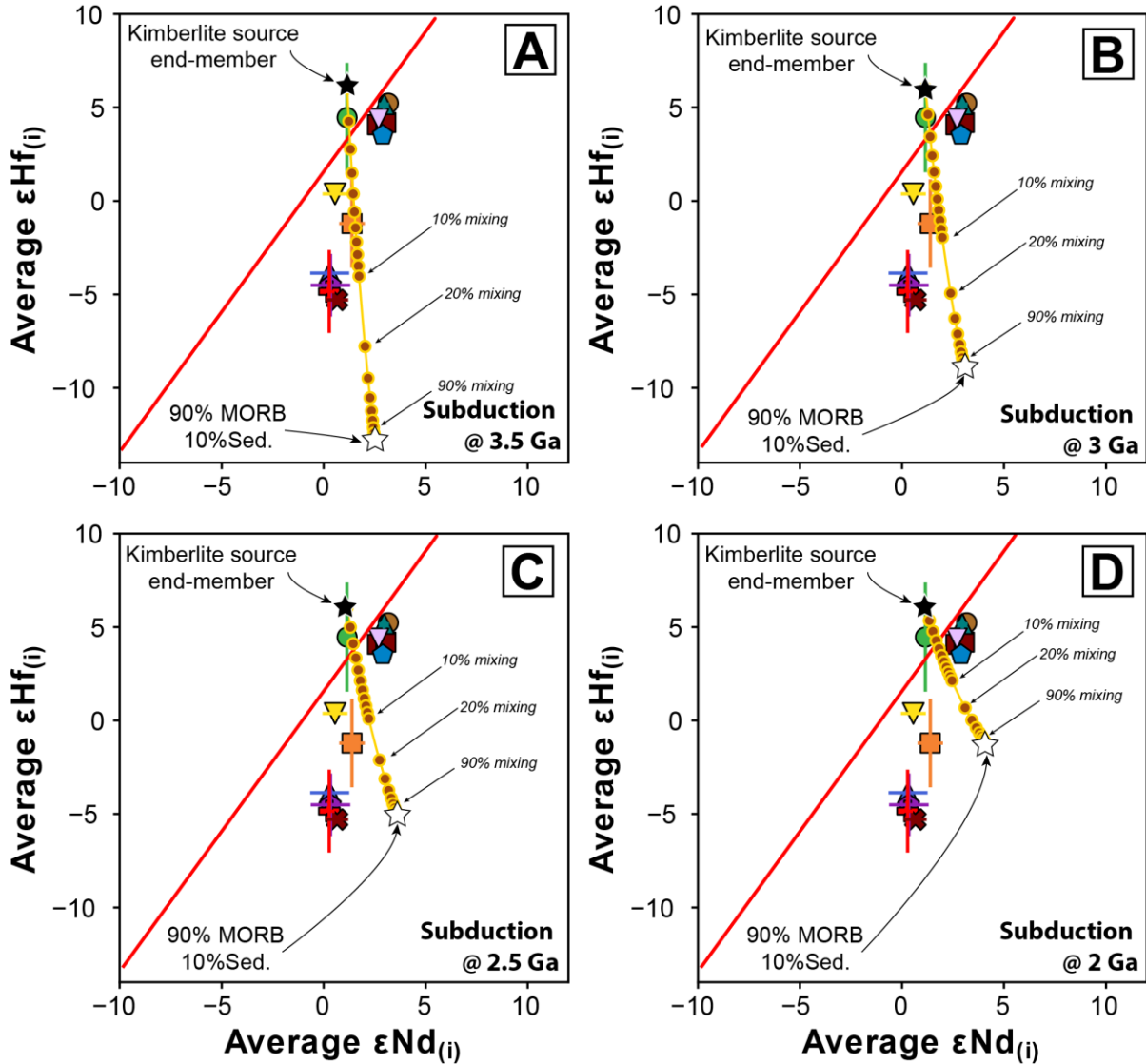
Supplementary Figure S5: $\epsilon Nd_{(i)}$ vs $^{87}Sr/^{86}Sr_{(i)}$ isotope composition of Kaavi-Kuopio kimberlites and entrained xenoliths and xenocrysts. Xenolith and xenocryst data are from Peltonen et al. (1999). Kimberlite literature data are from O'Brien and Tyni (1999).



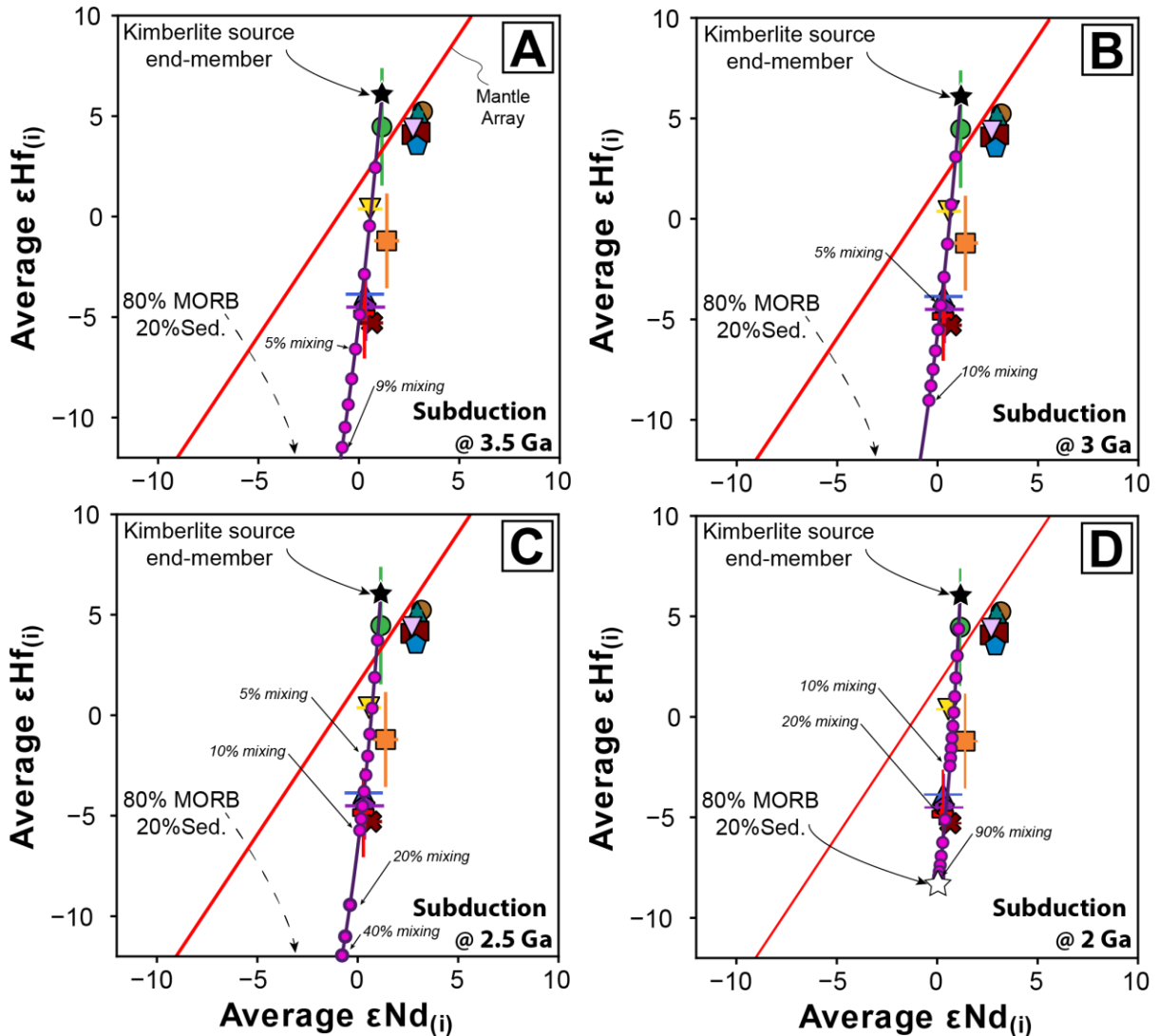
Supplementary Figure S6: Bivariate plot of $\epsilon\text{Hf}_{(i)}$ vs $\epsilon\text{Nd}_{(i)}$ for the Kaavi-Kuopio kimberlites showing binary mixing relationship between a primitive kimberlite source region and subducted material of various ages. A) Subduction at 3.5 Ga; B) Subduction at 2 Ga. Subducted material is composed of 100% MORB (Gale et al., 2013; Nowell et al., 2004). Compositions of subducted component adjusted to account for subduction-induced, sediment-fluid modification following Stracke et al. (2003). See Supplementary Table S2 for full model parameters.



Supplementary Figure S7: Bivariate plot of $\epsilon\text{Hf}_{(i)}$ vs $\epsilon\text{Nd}_{(i)}$ for the Kaavi-Kuopio kimberlites showing binary mixing relationship between a primitive kimberlite source region and subducted material of various ages. A) Subduction at 3.5 Ga; B) Subduction at 3 Ga; C) Subduction at 2.5 Ga; D) Subduction at 2 Ga. Subducted material is composed of 80% MORB (Gale et al., 2013; Nowell et al., 2004) and 20% Sediment (Sed.; GLOSS II of Plank, 2014). Compositions of subducted component adjusted to account for subduction-induced, sediment-fluid modification following Stracke et al. (2003). See Supplementary Table S2 for full model parameters.



Supplementary Figure S8: Bivariate plot of $\epsilon\text{Hf}_{(i)}$ vs $\epsilon\text{Nd}_{(i)}$ for the Kaavi-Kuopio kimberlites showing binary mixing relationship between a primitive kimberlite source region and subducted material of various ages. A) Subduction at 3.5 Ga; B) Subduction at 3 Ga; C) Subduction at 2.5 Ga; D) Subduction at 2 Ga. Subducted material is composed of 90% MORB (Gale et al., 2013; Nowell et al., 2004) and 10% Sediment (Sed.; coarse sediment of Bayon et al., 2009). Compositions of subducted component adjusted to account for subduction-induced, sediment-fluid modification following Stracke et al. (2003). See Supplementary Table S2 for full model parameters.



Supplementary Figure S9: Bivariate plot of $\epsilon\text{Hf}_{(i)}$ vs $\epsilon\text{Nd}_{(i)}$ for the Kaavi-Kuopio kimberlites showing binary mixing relationship between a primitive kimberlite source region and subducted material of various ages. A) Subduction at 3.5 Ga; B) Subduction at 3 Ga; C) Subduction at 2.5 Ga; D) Subduction at 2 Ga. Subducted material is composed of 80% MORB (Gale et al., 2013; Nowell et al., 2004) and 20% Sediment (Sed.; coarse sediment of Bayon et al., 2009). Compositions of subducted component adjusted to account for subduction-induced, sediment-fluid modification following Stracke et al. (2003). See Supplementary Table S2 for full model parameters.

Supplementary Table S1. Nd-Hf-Sr isotope results for samples in this study and results of thermometry calculations

Table provided in a separate file

Supplementary Table S2. Inputs for binary mixing models

Table provided in a separate file

Full dataset available via the University of Melbourne Figshare Repository:

[10.26188/c.5770949](https://doi.org/10.26188/c.5770949)

References

- Ballhaus, C., Berry, R.F., Green, D.H., 1994. High-pressure experimental calibration of the olivine-orthopyroxene-spinel oxygen geobarometer: implications for the oxidation state of the upper mantle. *Contributions to Mineralogy and Petrology*, 118(1): 109-109.
- Bayon, G. et al., 2009. Hf and Nd isotopes in marine sediments: Constraints on global silicate weathering. *Earth and Planetary Science Letters*, 277(3): 318-326.
- Dalton, H., Giuliani, A., O'Brien, H., Phillips, D., Hergt, J., 2020. The role of lithospheric heterogeneity on the composition of kimberlite magmas from a single field: The case of Kaavi-Kuopio, Finland. *Lithos*, 354-355: 105333.
- Fedortchouk, Y., Canil, D., 2004. Intensive Variables in Kimberlite Magmas, Lac de Gras, Canada and Implications for Diamond Survival. *Journal of Petrology*, 45(9): 1725-1745.
- Gale, A., Dalton, C.A., Langmuir, C.H., Su, Y., Schilling, J.-G., 2013. The mean composition of ocean ridge basalts. *Lithos*, 14(3): 489-518.
- Giuliani, A. et al., 2020. Kimberlite genesis from a common carbonate-rich primary melt modified by lithospheric mantle assimilation. *Science Advances*, 6(14).
- Kavanagh, J.L., Sparks, R.S.J., 2009. Temperature changes in ascending kimberlite magma. *Earth and Planetary Science Letters*, 286(3): 404-413.
- Lehtonen, M., O'Brien, H., 2009. Mantle transect of the Karelian Craton from margin to core based on PT data from garnet and clinopyroxene xenocrysts in kimberlites. *Bull. Geol. Soc. Finland*, 81: 79-102.
- Mather, K.A., Pearson, D.G., McKenzie, D., Kjarsgaard, B.A., Priestley, K., 2011. Constraints on the depth and thermal history of cratonic lithosphere from peridotite xenoliths, xenocrysts and seismology. *Lithos*, 125(1): 729-742.
- Nimis, P., Taylor, W.R., 2000. Single clinopyroxene thermobarometry for garnet peridotites. Part I. Calibration and testing of a Cr-in-Cpx barometer and an enstatite-in-Cpx thermometer. *Contributions to Mineralogy and Petrology*, 139(5): 541-554.

- Nowell, G.M. et al., 2004. Hf Isotope Systematics of Kimberlites and their Megacrysts: New Constraints on their Source Regions. *Journal of Petrology*, 45(8): 1583-1612.
- O'Brien, H.E., Tyni, M., 1999. Mineralogy and geochemistry of kimberlites and related rocks from Finland, Proceedings of the 7th international kimberlite conference. Red Roof Design cc Cape Town, South Africa, pp. 625-36.
- O'Neill, H.S.C., Wall, V., 1987. The Olivine—Orthopyroxene—Spinel oxygen geobarometer, the nickel precipitation curve, and the oxygen fugacity of the Earth's Upper Mantle. *Journal of Petrology*, 28(6): 1169-1191.
- Peltonen, P., Huhma, H., Tyni, M., Shimizu, N., 1999. Garnet peridotite xenoliths from kimberlites of Finland: nature of the continental mantle at an Archaean craton—Proterozoic mobile belt transition, Proceedings of the 7th International Kimberlite Conference. Red Roof Design cc Cape Town, South Africa, pp. 664-676.
- Plank, T., 2014. The Chemical Composition of Subducting Sediments. In: Holland, H.D., Turekian, K.K. (Eds.), *Treatise on Geochemistry (Second Edition)*. Elsevier, Oxford, pp. 607-629.
- Stracke, A., Bizimis, M., Salters, V.J.M., 2003. Recycling oceanic crust: Quantitative constraints. *Geochemistry, Geophysics, Geosystems*, 4(3).
- Tappe, S., Stracke, A., van Acken, D., Strauss, H., Luguet, A., 2020. Origins of kimberlites and carbonatites during continental collision – Insights beyond decoupled Nd-Hf isotopes. *Earth-Science Reviews*: 103287.
- Tovey, M. et al., 2021. The spatial and temporal evolution of primitive melt compositions within the Lac de Gras kimberlite field, Canada: Source evolution vs lithospheric mantle assimilation. *Lithos*, 392-393: 106142.